Geophys. J. Int. (1996) **125**, 355–370

Application of very fast simulated annealing to the determination of the crustal structure beneath Tibet

Lian-She Zhao, Mrinal K. Sen, Paul Stoffa and Cliff Frohlich

Institute for Geophysics, The University of Texas at Austin, 8701 N. MoPac Expressway, Austin, TX 78759-8397, USA

Accepted 1995 October 23. Received 1995 October 18; in original form 1995 July 13

SUMMARY

The simulated annealing method has recently been applied to several multiparameter optimization problems, including those of geophysical inversion. A new variant of simulated annealing, called very fast simulated annealing (VFSA), overcomes some of the drawbacks of a conventional simulated annealing; it has been found to be a practical tool for geophysical inversion (Sen & Stoffa 1995). The method is particularly useful for non-linear problems with multiple parameters where a grid-search method is prohibitively expensive. Here, we have applied VFSA to retrieve the crustal structure beneath seismic stations in Tibet using teleseismic body-waveform data. Our approach is to compare the radial-component records with generalized ray synthetics directly in the time domain. For any given crustal structure, we have formulated a direct relationship between the radial- and the vertical-component signal, so that we can generate synthetic radial-component data from recorded vertical-component seismograms (Zhao & Frohlich 1996). We have tested the VFSA inversion algorithm using synthetics and confirmed that it works very well, i.e. it finds solutions very close to the true solution. Using the algorithm, we have determined the crustal structures beneath 11 stations in Tibet. From south to north, the total crustal thickness is quite uniform. Our tectonic interpretation of these crustal models is that they may represent crust from the Eurasian plate injected beneath the crust of the converging Indian plate. Certain features of the models are consistent with the presence of a small convection cell or plume beneath north–central Tibet, as suggested by Molnar (1990).

Key words: crustal structure, inversion, Tibet.

INTRODUCTION

Since Phinney (1964) noticed that teleseismic body waveforms provide constraints on the velocity structure beneath seismic stations, there have been numerous papers on his transfer function methods [see Båth (1974) for a review]. Langston (1979) introduced the concept of receiver functions, as they were later called, which were both a variation and an improvement on Phinney's transfer function. Owens, Zandt & Taylor (1984) posed the receiver function problem as an inverse problem and used the difference in waveforms as partial derivatives. Zhao & Frohlich (1996) used grid-search methods to find crustal models which provided the optimal fit in the time domain between radial-component synthetics and observations. The grid-search approach was practical because they employed several techniques that made the construction of synthetics very efficient. They showed that a second-order expansion of ratios of radial- and vertical-component signals (the SORVEC method) was sufficiently accurate for constructing radial-component synthetics, and they also demonstrated that one could use a few rays to generate a reasonably complete synthetic seismogram.

In this paper, we apply the global optimization method of very fast simulated annealing (VFSA) to the SORVEC method. We shall briefly describe SORVEC and the VFSA inversion method and then present the results of our inversions for crustal structure. We use the VFSA algorithm to determine crustal structure beneath Tibet at one permanent station (LSA, Lhasa) and 10 temporary stations (Owens *et al.* 1993). For most regions in Tibet, the crustal structure is poorly known, and what little is known is derived from analysis of surface waveforms. For example, Zhao, Helmberger & Harkrider (1991) derived a crustal model using Love waveforms, but only had the data paths for southern Tibet. However, Zhu *et al.* (1993) studied the receiver structures of stations TUNL, WNDO and XIGA, using a receiver-function method. Zhao & Frohlich (1996) reported preliminary results concerning crustal structure beneath two stations in Tibet.

SORVEC

SORVEC (second-order radial vertical comparison) was developed recently by Zhao & Frohlich (1996). Using the SORVEC method, we can generate radial-component synthetics from given crustal and uppermost-mantle structure, and vertical component records for body-wave waveforms at teleseismic distances.

Assuming that the P signal arriving at the base of the crust from a teleseismic event is $S(t)$, which includes both the source signal and complexity caused by near-source structure, we can write the observed vertical-component seismogram $Z(t)$ and radial-component seismogram $H(t)$ as

$$Z(t)=z_0S(t)+\sum_i z_iS(t-t_i)$$

and

$$H(t)=r_0S(t)+\sum_i r_iS(t-t_i),$$

where z_i and r_i are the appropriate products of receiver responses and transmission and reflection coefficients from the Moho to the free surface along the ray path. The t_i are the time delays for reflected and converted rays in the crust.

It was proved that the normalized horizontal component can be expressed in terms of the normalized vertical component (Zhao & Frohlich 1996):

$$H(t)\cong Z(t)+\sum_i \frac{r_i}{r_0} Z(t-t_i) \quad \text{(0th order)},$$

$$\cong Z(t)+\sum_i \left(\frac{r_i}{r_0}-\frac{z_i}{z_0}\right) Z(t-t_i) \quad \text{(1st order)},$$

$$\cong Z(t)+\sum_i \left(\frac{r_i}{r_0}-\frac{z_i}{z_0}\right) [Z(t-t_i)-Y_2(t-t_i)] \quad \text{(2nd order)},$$

$$\cong Z(t)+\sum_i \left(\frac{r_i}{r_0}-\frac{z_i}{z_0}\right) [Z(t-t_i)-Y_2(t-t_i)-\ldots-Y_n(t-t_i)] \quad \text{(nth order)},$$

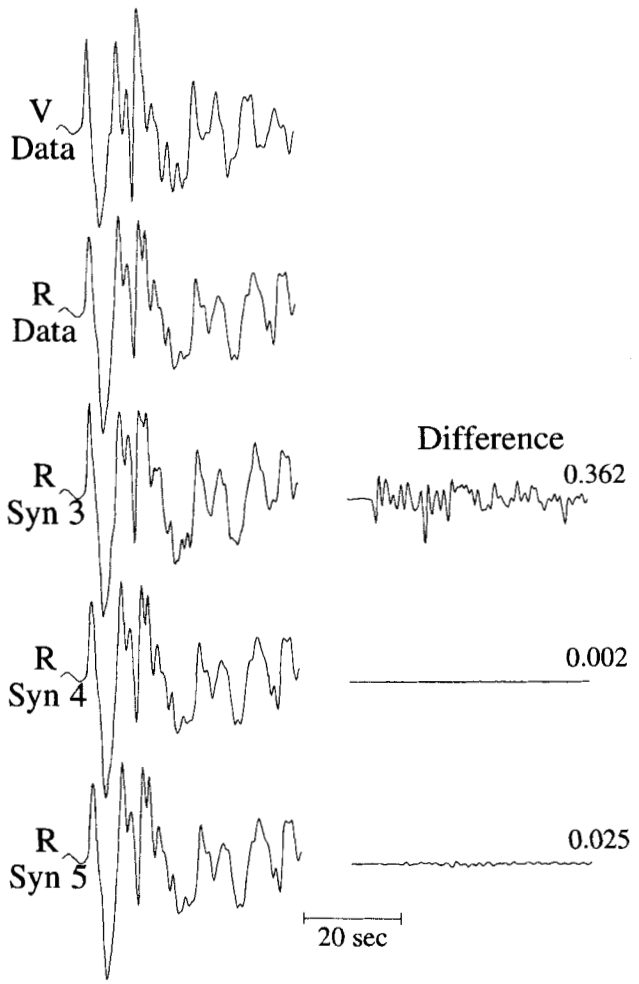

Figure 1. Comparison of radial-component synthetic data with synthetics generated for different classes of crustal models with the SORVEC method. Here we use the signal labelled 'V' (vertical component of a P wave recorded at station MAQI from an earthquake occurring on 1992 February 17 as input for SORVEC to generate a radial-component signal, 'R', using the four-layer-over-halfspace 'Input' crustal model in Table 1. We test the VFSA inversion method by searching to find the best-fitting crustal models having three, four and five layers (see Table 1) and the associated radial-component synthetics (labelled 'Syn 3', 'Syn 4' and 'Syn 5'). The 'Difference' column is the difference between the 'Radial' signal for the 'Input' crustal structure and the synthetics generated for the best-fitting models; the numbers on the right are the misfit, i.e. the amplitude of difference as a fraction of the maximum amplitude of the radial component. Note that the fits for all of these models are excellent.

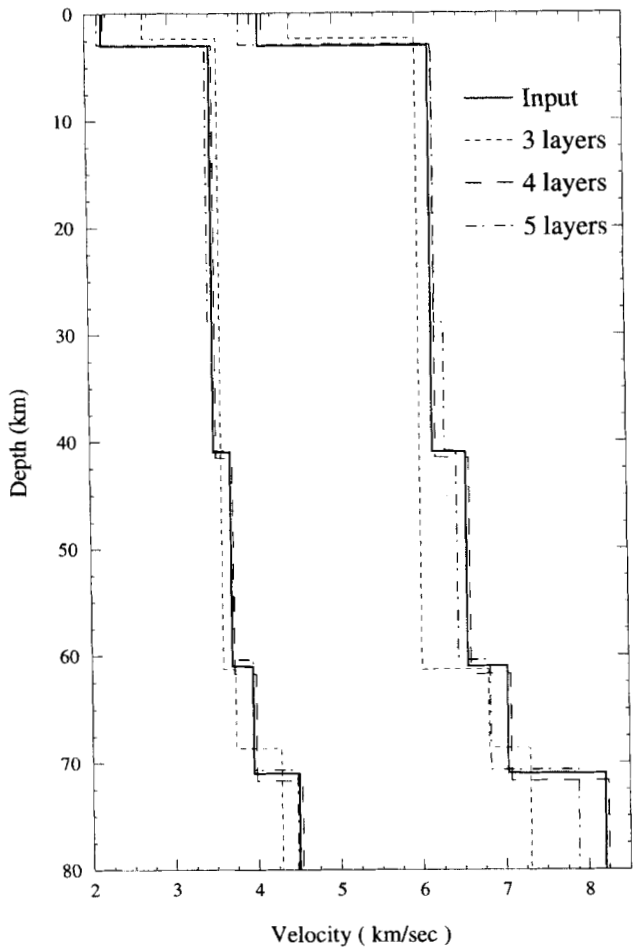

Figure 2. For the example shown in Fig. 1, a comparison of P and S velocities for the 'Input' model (solid line) with the best-fitting three-, four- and five-layer models determined using the VFSA program.

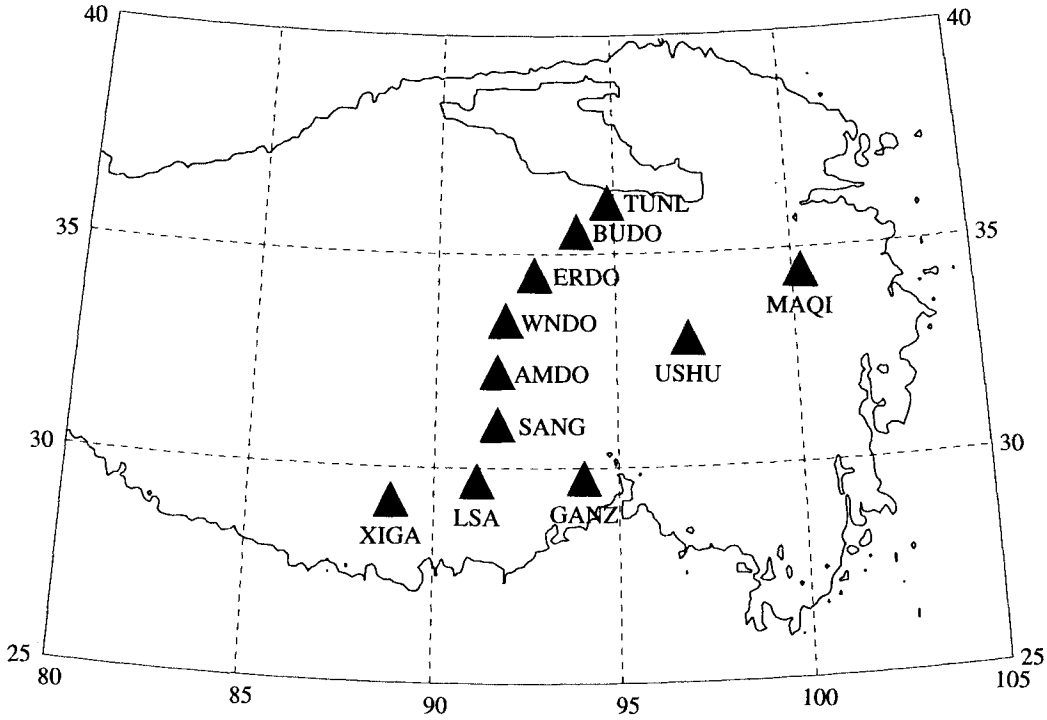

Figure 3. Location map of stations (triangles) evaluated in this study. The solid lines are 3000 m contour lines, which approximately indicate the boundary of Tibet.

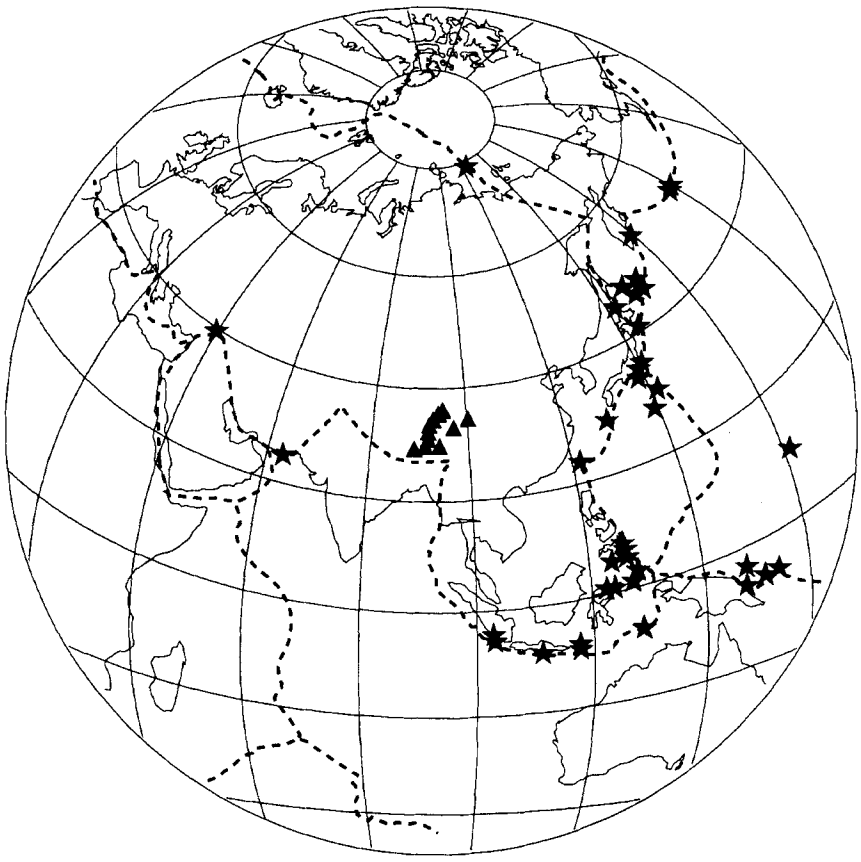

Figure 4. Location map of earthquakes (stars) and stations (triangles) evaluated in this study.

where

$$Y_2(t)=\sum_i \frac{z_i}{z_0} Z(t-t_i),$$

$$Y_n(t)=-\sum_i \frac{z_i}{z_0} Y_{n-1}(t-t_i).$$

The second-order expression gives good approximation up to within a few per cent (Zhao & Frohlich 1996), thus we used the second-order, and hence the SORVEC name. For a detailed derivation and its performance, see Zhao & Frohlich (1996).

VERY FAST SIMULATED ANNEALING

The inversion for receiver structure by waveform fitting is an optimization problem in which we attempt to minimize a measure of misfit, i.e. an error function. There exist several approaches to optimizing a multidimensional functional. The traditional gradient-based approaches (e.g. Tarantola 1987) calculate an update to a current model assuming that the error function is locally linear. Such methods do not work when the error surface is characterized by several hills and valleys. A grid-search method overcomes this problem (e.g. Zhao & Frohlich 1996). However, the accuracy of the method depends on the discrete grid size, and the computational costs become prohibitive when the model space becomes very large. Pure Monte Carlo random search techniques are directionless and are not guaranteed to find the optimum answer. For this reason, directed Monte Carlo methods, such as simulated annealing (SA) and genetic algorithms (GA), have recently gained popularity in the geophysical community (e.g. Rothman 1985; Sen & Stoffa 1991; Stoffa & Sen 1991). Sen & Stoffa (1995) present a detailed description of these methods, along with examples of several geophysical applications.

The SA method (Metropolis *et al.* 1953) has been applied to a variety of optimization problems. The Metropolis algorithm, as used by Kirkpatrick, Gelatt & Vecchi (1983), involves the following steps.

(1) Random selection of an initial model (m_i) from a predetermined model space. This requires setting the search limits of each one of the model parameters. In our problem this will mean assigning minimum and maximum values for compressional-wave velocity, shear-wave velocity and layer thickness.

(2) Evaluation of an error function [$E(m_i)$], which can be defined as a function of the difference between the observed and synthetic seismograms (eq. 10, Zhao & Frohlich 1996).

(3) Perturbation of the initial model to model m_j, then evaluation of $E(m_j)$ and $\Delta E=E(m_i)-E(m_j)$.

(4) If $\Delta E<0$, accept m_j. If $\Delta E>0$, accept m_j with a probability $\exp(-\Delta E/T)$, where T is a control parameter called temperature.

The SA procedure involves repeating steps (1) to (4) a large number of times with a constant value for T. Then, we lower T following a cooling schedule, and repeat this procedure a large number of times until the error no longer changes. Although this seems like a very difficult task, experience shows it is much more efficient than an exhaustive search.

Recently, Ingber (1989) proposed a modification of the Metropolis SA method called very fast simulated annealing (VFSA), which is very efficient for many geophysical applications. Whereas the Metropolis SA method chooses new models randomly from the entire model space for comparison with the current model, the VFSA method chooses new models using a Cauchy-like distribution function, which depends on the current model and on temperature T (called model temperature), which is lowered at subsequent iterations. This allows for a wide search of the model space during initial iterations and a narrower search as one approaches the optimum solution. This search scheme also allows for the use of a very fast cooling schedule, which is why the method is so efficient compared with other SA and GA methods.

EVALUATION OF THE ALGORITHM WITH SYNTHETIC DATA

We have developed a VFSA inversion algorithm to determine crustal structure beneath seismic stations. This algorithm utilizes the misfit function described in Zhao & Frohlich (1996) to compare recorded teleseismic signals with synthetic data generated using the SORVEC method. Our tests indicate that the inversion algorithm successfully recovers input crustal structure in trial situations. We used real vertical-component data recorded at station MAQI in Tibet from an earthquake in northern Asia to calculate a radial-component seismogram for a trial four-layer input crustal structure (Fig. 1 and Table 1). Then, we applied the VFSA algorithm to these data to determine the best-fitting three-, four- and five-layer crustal models (Fig. 2 and Table 1). Note that the four- and five-layer models recovered are both similar to the input model and have much better fits ($\leq$0.025; Fig. 1) than the three-layer model (0.362); also note that the best-fitting five-layer model is nearly the same as the four-layer model, except that the second layer is split into two layers with nearly the same velocities.

This test (Figs 1 and 2) demonstrates that the performance of the VFSA algorithm is satisfactory, even though we have used excessively wide ranges for the permissible model parameters (last two columns, Table 1). Moreover, even though we chose starting models at random from the search windows in

Table 1. Models for testing VFSA.

	Input	3 Layers	4 Layers	5 Layers	Minimum	Maximum
	α, β, Th	α, β, Th	α, β, Th	α, β, Th	α, β, Th	α, β, Th
	4.10 2.20 3	4.48 2.70 2.33	4.15 2.22 2.97	3.87 2.15 2.91	3.2 1.8 1	7.5 3.8 20
	6.15 3.50 26	6.00 3.59 26.0	6.19 3.53 26.0	6.20 3.45 26.0	3.2 1.8 1	7.5 3.8 60
Crust	6.15 3.50 12	6.00 3.59 12.0	6.19 3.53 12.6	6.30 3.50 11.9	3.2 1.8 1	7.5 3.8 40
	6.55 3.70 20	6.00 3.59 21.0	6.59 3.73 20.2	6.44 3.70 19.5	3.2 1.8 1	7.5 4.0 20
	7.03 3.95 10	6.80 3.74 7.34	7.07 3.99 9.96	6.82 3.95 10.3	3.2 1.8 1	7.5 4.0 20
Mantle	8.20 4.50 -	7.30 4.29 -	8.24 4.54 -	7.88 4.48 -	7.3 4.2 1	8.9 4.8 1

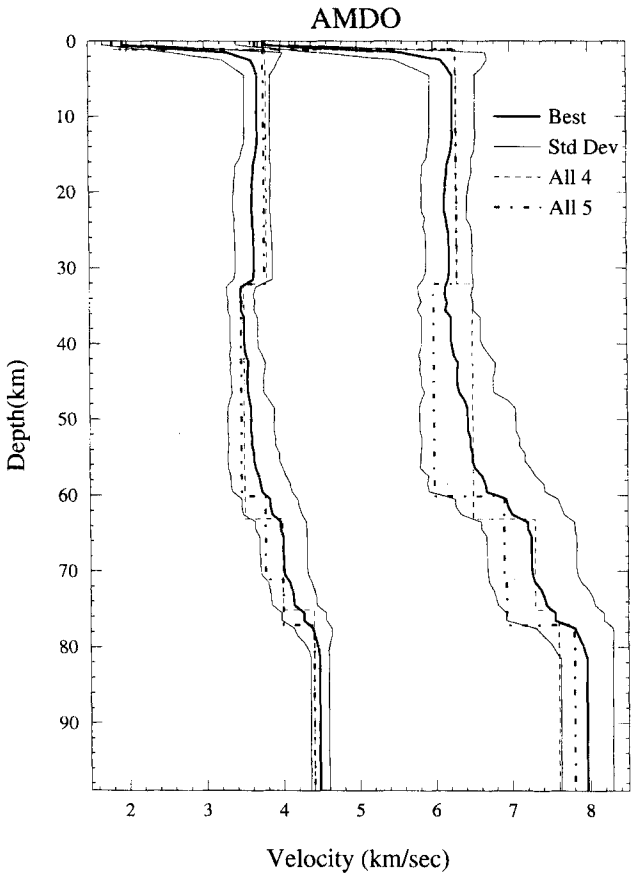

Figure 5. Velocity models obtained for station AMDO. 'Best' and 'Std Dev' indicate the mean and standard deviation of all models found from the VFSA inversion of individual earthquake-station waveform data; 'All 4' and 'All 5' are the optimum four- and five-layer models determined from a simultaneous inversion of all available waveforms.

Table 2. Station locations.

Station	Location (°N, °E)	
AMDO	32.247	91.688
BUDO	35.529	93.910
ERDO	34.520	92.707
GANZ	29.767	94.050
LSA	29.700	91.150
MAQI	34.478	100.249
SANG	31.024	91.700
TUNL	36.199	94.815
USHU	33.011	97.015
WNDO	33.448	91.904
XIGA	29.234	88.851

these tests, the VFSA algorithm was able to find a crustal structure that is very close to the trial input crustal model.

APPLICATION TO TIBETAN STATIONS

We applied the VFSA algorithm to determine the crustal structure beneath 10 Tibet-PASSCAL stations and the Chinese digital station LSA (Fig. 3 and Table 2). The range for search parameters in the VFSA inversion was the same as used in the example above (see Table 1). Altogether, about 50 earthquakes (Fig. 4 and Table 3) recorded at distances of 30° to 70° provided the data for the inversion. The azimuthal coverage is much better in the east of Tibet than in the west (Fig. 4), where there are only two earthquakes with recordings of reasonable quality. There are no events in the southwestern quadrant at all.

For processing the seismic waveforms analysed in this paper, we used NEIC locations and assumed that seismic waves arriving at the base of the crust possessed a ray parameter consistent with the IASP91 model (Kennett & Engdahl 1991). This is an adequate assumption for this type of analysis, since ray-parameter differences are quite small among different velocity models or for slightly different station–event distances: at 45° distance the ray parameters of the JB and IASP91 models differ by less than 0.3 per cent and they vary by less than 1 per cent per degree distance.

Table 3. Events used for 10 PASSCAL stations.

ID	Date mmddyy	Time hhmm	Location (°N, °E)		Depth (km)	Mag (M_b)
013	010392	1158	1.342	127.373	113	6.0
020	012092	1337	27.983	139.405	499	5.8
030	013092	0522	24.958	63.141	29	5.5
032	020192	1904	35.106	139.644	100	5.6
048	021792	0001	79.191	124.482	10	5.9
064	030492	0349	-3.008	147.882	19	6.0
065	030592	1439	52.900	159.619	45	6.3
073	031392	1718	39.710	39.605	27	6.2
084	032492	1719	-7.751	117.464	280	5.5
086	032692	1414	51.222	-179.723	33	5.9
087	032792	2028	47.863	147.128	454	5.5
094	040392	0319	-5.696	151.164	27	5.8
107	041692	0800	1.186	122.586	30	5.6
109	041892	0916	-5.454	103.001	29	5.7
110	041992	1832	23.861	121.594	16	5.8
119	042892	0155	5.602	124.054	477	5.5
128	050792	0623	41.175	144.700	13	5.8
136	051592	0705	-6.075	147.572	58	6.2
138	051792	0949	7.239	126.645	33	6.2
142	052192	1805	-8.748	117.604	143	5.7
152	053192	0620	30.640	141.596	32	5.6
155	060392	0610	51.130	178.743	22	5.9
158	060692	2140	1.068	124.040	18	5.9
161	060992	0031	-8.474	111.100	64	5.9
168	061692	0551	45.704	142.263	317	5.7
202	072191	2259	3.008	128.434	34	5.9
215	080391	0833	29.330	129.081	17	5.5
218	080691	1449	35.725	141.044	29	5.9
246	090391	0844	33.649	138.778	27	5.9
275	100291	1432	-10.402	161.363	91	5.4
281	100891	0331	45.587	149.049	146	6.0
303	103091	0402	-5.657	153.899	69	5.7
311	110791	0921	-7.320	128.550	140	5.9
312	110891	1712	-4.273	102.806	80	5.7
317	111391	1112	8.361	126.371	36	6.1
325	112191	1238	5.782	126.832	73	6.0
347	121391	0012	-7.270	128.621	159	5.6
347	121391	0233	45.578	151.560	30	6.1
351	121791	0638	47.393	151.499	157	5.8

Because the seismic velocity beneath Tibet may be quite complicated and because we wanted to focus on the major structural features, we filtered the waveforms so that they resembled recordings on a long-period Press–Ewing instrument. Individual waveforms included about 40–50 s of signal following the initial *P* arrival, thus the data can resolve crustal thicknesses of up to about 80 km. This is a reasonable maximum for Tibet, as evidenced from other studies, such as gravity and deep seismic sounding. To constrain the crustal thickness to within reasonable values, in our inversions we fixed the lower limit of the mantle shear velocity to be 4.4 km s^{-1}.

For each individual earthquake–station pair, the data consist of a vertical-component and a radial-component waveform; to these data we applied the VFSA algorithm twice, obtaining the best-fitting crustal models with four layers over a half-space and with five layers over a half-space. In addition, at each station we used all the available waveform data together in a single inversion, obtaining the best-fitting four-layer and five-layer models (labelled 'All' in Table 4, Fig. 5 and subsequent figures). Thus, beneath each station we found a suite of different velocity models, with each model optimized for the particular earthquake waveforms used in the inversion.

Finally, at each station we also determined an average model (labelled 'Best' in Fig. 5 and subsequent figures) and its standard deviation by forming, at each depth, the mean and standard deviation of *P* and *S* velocities determined from each of the individual earthquake–station data inversions and the inversions using all data traces. The weight of a given model used in the determination of the average model and its standard deviation is the number of data traces used to determine this model. Note that this 'Best' model may not provide better fits of data than the best models from individual runs. However, the 'Best' model, an average of all the individual models obtained, should be a better representation of the velocity structure beneath the station. For each station we display the average model and its deviation, and the models derived using all data traces available (e.g. Fig. 5). It is unlikely that the velocity beneath any particular station lies outside the range indicated, i.e. the average $\pm$ the standard deviation. To illustrate the details of this process, at one station only, AMDO, we present a table (Table 4) of the entire suite of velocity models found in the inversion, along with examples of the waveform fits (Fig. 6). We will not give detailed information for waveform fitting for stations other than AMDO and LSA; to give an idea of the fit we will show how many records are of good quality, by which we mean those with ≤ 0.4 for the amplitude of the difference between data and synthetics, and how many are 'noisy', by which we mean those ≥ 0.5 for the amplitude of the difference.

Station AMDO

Beneath station AMDO, the principal results of our VFSA analysis are that there is a low-velocity layer beneath about 30 km depth, and that the total crustal thickness is about 65–80 km (Fig. 5 and Table 4). In the upper crust at depths of 5–15 km, the velocity is well constrained, with an uncertainty of about ± 0.2 km s^{-1} for shear velocity (Fig. 5). The uncertainty is somewhat larger at greater depths. The shear velocity for the upper 30 km beneath the surface is 3.6–3.7 km s^{-1}, compared to 3.4–3.5 km s^{-1} in the lower-velocity region below. The depth of the Moho is not well constrained, but it clearly lies between

Table 4. Models for station AMDO.

Ev	Baz	Layer 1	Layer 2	Layer 3	Layer 4	Layer 5	Mantle	err
		α, β, Th	α, β, Th	α, β, Th	α, β, Th	α, β, Th	α, β	
All		3.70 1.81 1.1	6.30 3.80 31	6.50 3.53 31	7.30 3.97 12		7.63 4.40	13.4
086	44	3.40 2.05 2.3	6.22 3.69 38	5.50 3.40 22	7.30 3.97 13		8.19 4.40	7.7
351	53	3.67 1.80 1.2	5.51 3.28 14	5.60 3.43 32	6.90 3.77 32		8.20 4.44	17.2
128	62	4.00 1.96 1.5	6.61 3.80 31	6.19 3.42 26	6.90 3.95 19		7.80 4.50	2.7
218	71	3.64 2.16 4.3	6.78 3.73 14	5.91 3.25 22	6.74 3.74 14		8.20 4.55	11.1
020	83	3.30 1.95 1.8	6.14 3.45 32	6.68 3.61 26	6.70 3.98 14		8.20 4.40	7.5
110	100	3.87 1.90 1.9	6.67 3.61 18	5.90 3.23 20	6.80 3.65 20		8.20 4.45	5.8
094	112	4.15 2.26 1.8	6.59 3.55 14	6.28 3.46 36	7.00 3.81 18		7.73 4.44	3.2
202	122	3.90 1.92 1.2	6.33 3.80 31	6.16 3.50 26	6.51 3.83 15		8.60 4.64	12.9
311	132	4.60 2.45 3.3	6.64 3.80 12	6.00 3.25 27	7.20 3.90 15		7.65 4.40	10.4
142	144	3.70 2.21 2.8	5.96 3.39 40	5.60 3.06 22	6.60 3.93 12		8.30 4.80	18.1
109	161	3.40 1.90 1.3	6.10 3.65 34	5.58 3.24 22	6.50 3.55 22		7.64 4.45	4.3
275	180	3.70 1.83 1.1	5.20 3.13 22	6.48 3.79 14	6.50 3.88 10		8.90 4.77	18.1
073	295	5.15 2.97 1.0	6.10 3.60 15	5.30 3.01 20	6.98 4.00 22		8.81 4.75	14.1
All		3.66 1.81 1.1	6.30 3.77 31	5.99 3.46 28	6.90 3.77 11	6.93 4.00 6	7.80 4.40	13.3
086	44	3.23 1.82 2.1	6.13 3.57 12	5.70 3.15 30	6.60 3.57 12	6.70 3.95 5	8.02 4.45	7.4
351	53	3.61 1.82 1.3	5.90 3.55 30	5.29 3.15 15	6.60 3.55 13	6.77 3.79 19	8.31 4.51	16.6
128	63	3.73 1.86 1.2	6.35 3.68 31	6.10 3.38 20	6.50 3.50 5	7.30 3.98 18	8.00 4.60	2.7
218	71	3.61 1.83 1.3	6.40 3.78 12	6.00 3.60 11	7.23 4.00 9	6.79 3.65 8	7.88 4.41	10.9
020	83	3.50 2.09 2.2	6.09 3.39 31	6.56 3.55 12	6.62 3.62 14	6.70 3.99 13	8.20 4.41	7.2
110	100	3.49 1.81 1.7	6.79 3.76 17	6.39 3.45 23	7.05 3.99 5	7.00 3.80 15	8.00 4.60	5.6
094	112	4.11 2.40 2.0	6.41 3.61 12	6.20 3.42 22	6.60 3.55 16	7.27 3.95 19	8.50 4.60	2.9
202	122	4.20 2.12 1.4	6.31 3.80 23	5.78 3.40 33	6.75 3.69 8	6.55 3.83 7	8.59 4.65	12.9
311	132	3.69 1.81 1.4	6.74 3.80 14	6.10 3.39 27	6.70 3.64 12	6.70 4.00 11	8.20 4.40	9.8
142	144	4.10 2.07 2.4	5.52 3.14 32	6.30 3.80 16	6.50 3.50 18	6.72 4.00 13	8.41 4.80	18.7
109	161	3.49 1.94 1.3	6.20 3.72 34	5.40 3.29 22	6.60 3.55 15	6.80 3.68 8	8.24 4.58	4.2
275	180	4.00 2.01 1.3	5.60 3.45 11	5.50 3.37 13	6.70 3.99 18	6.52 3.73 5	8.34 4.76	18.4
073	295	5.08 2.97 1.6	5.90 3.50 14	5.50 3.00 20	7.30 4.00 8	6.50 3.53 12	8.20 4.44	13.0

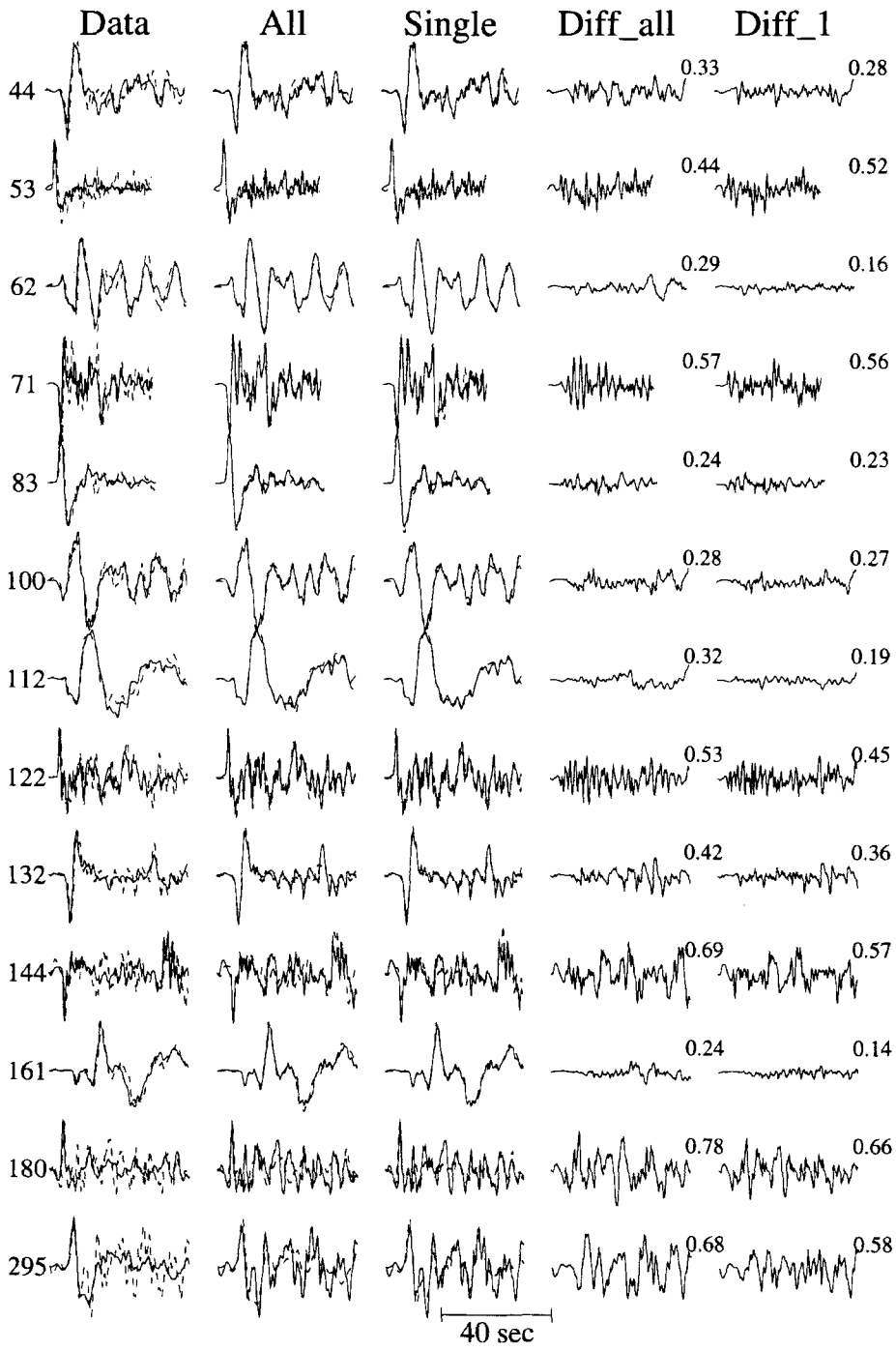

Figure 6. Comparison of observed and synthetic waveforms at station AMDO for earthquakes at different back azimuths (numbers at left). The 'Data' column depicts vertical-component (solid line) and radial-component (dashed line) observations. The 'All' column represents radial-component observations (solid lines) and synthetics (dashed lines) produced using the optimum four-layer crustal model determined by inverting all available waveform data. The 'Single' column similarly presents observations and synthetics obtained using the model determined by inverting the data in the left hand 'Data' column. 'Diff_all' and 'Diff_1' are the differences between the radial-component observations and the synthetics in the 'All' and 'Single' columns, respectively. The numbers to the right of the 'Diff_all' and 'Diff_1' columns are the peak trace amplitude, expressed as a fraction of the peak amplitude of the radial-component data.

about 65 km and 80 km. The mantle appears to have a rather low shear velocity, of the order of 4.5 km s^{-1} or less at a depth of 80 km. However, the uncertainty is large as the velocities considered are constrained by the 4.4 km s^{-1} lower limit of our search. Overall, the data constrain shear velocities in the crust more precisely than the compressional velocities.

Zhao & Frohlich (1996) evaluated the six backazimuths (44°, 83°, 122°, 161°, 180°, 295°) of data from the AMDO station using a grid-search algorithm to search for four-layer crustal models. Good agreements with almost all the details were achieved for models of 'all', 44°, 295°, 162° (velocities of the second layer of grid-search results are lower) and 181°

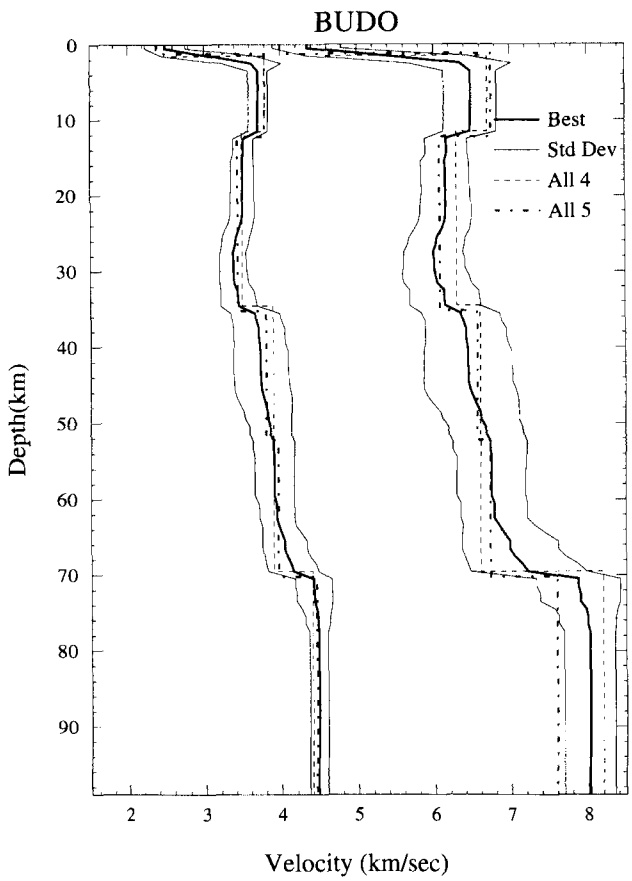

Figure 7. Velocity models obtained for station BUDO.

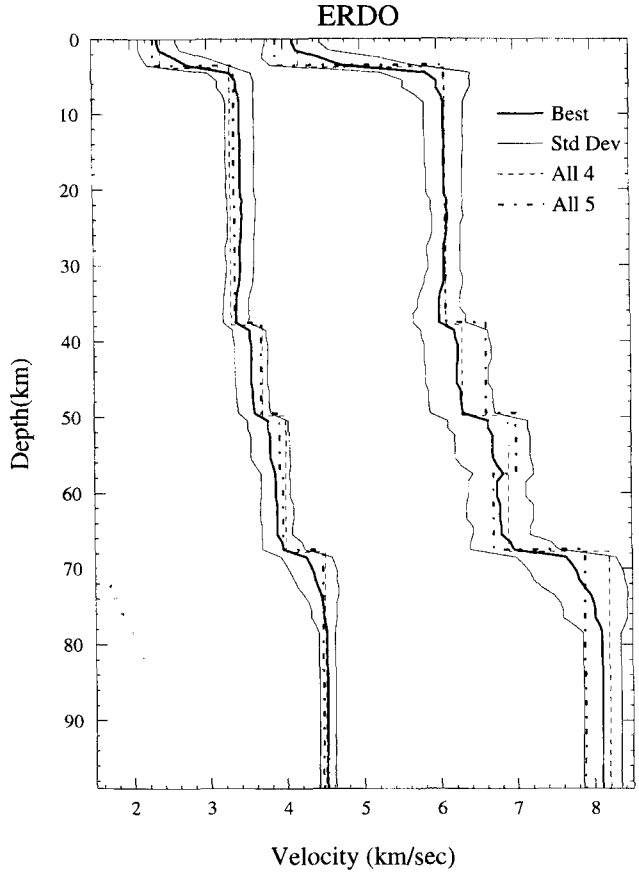

Figure 8. Velocity models obtained for station ERDO.

(velocities of the fourth layer of grid-search results are lower). The synthetics match the trend of the data, but the grid search gives lower velocities for the lower crust. The result for the model of 83° gives the worst comparison: the grid search suggests a low-velocity zone in the lower crust, but the VFSA does not. Generally, the VFSA results agree very well with the grid-search results. Note that the resolution is lower for the mantle velocities.

For most earthquakes, the fit between the radial-component observations and the synthetics expected for the best-fitting crustal models is generally acceptable (Fig. 6). For the models determined from individual waveforms, six possess maximum amplitude differences of 0.3 or less, whereas five have maximum amplitude differences of 0.6 or greater (e.g. see the backazimuths of 180° and 295°). Generally the fit is poorer when the signals are rich in high frequencies; however, this is unsurprising as it is the lower-frequency components that constrain the gross features of crustal structure. In most cases, the fits to models determined from individual waveforms are better than the fits to the 'All' models utilizing the entire data set. Nevertheless, the 'All' models are in some sense more reliable, as the use of many signals enhances the signal-to-noise ratio, especially when signals have roughly the same ray parameter.

Station BUDO

Station BUDO is located in north-central Tibet, where Zhao & Xie (1993) found the P_n velocity to be about 8.0 km s^{-1}. There are no previous measurements of crustal thickness for this area. We have collected 12 records having backazimuths from 45°–166° and one record from an earthquake at 292°. Most of the records are of good quality; only three are somewhat noisy.

Beneath BUDO, the principal results of our analysis are that there is a low-velocity region beneath about 12 km depth, and that the overall crustal thickness is about 70 km (Fig. 7). The resolution for shear velocity is quite good, especially at depths shallower than about 30 km. At the very top of the crust there is a low-velocity layer about 2 km thick, and below this there is a roughly homogeneous layer about 10 km thick where the shear velocity is about 3.70 km s^{-1}. The shear velocity at 12 km depth is about 3.5 km s^{-1}, and drops to less than 3.4 km s^{-1} at a depth of 25 km. Beneath this depth the velocity increases roughly linearly down to about 70 km. There is little question that the low-velocity layer in the upper crust is real, and that the uncertainty in the total crustal thickness is quite small—only a few kilometres. The mantle P velocity of 8.0 km s^{-1} is not well determined (e.g. see Zhao & Frohlich 1996). We have here determined a mantle shear velocity of 4.5 ± 0.1 km s^{-1}, lower than that obtained previously from modelling of *SH* waveforms (TIP, Zhao *et al.* 1991). Presumably this is because *SH* waveforms are of a longer period and sample deeper, and because model TIP is derived for the whole of Tibet.

Station ERDO

Little is known about the velocity structure beneath ERDO, which lies just southwest of station BUDO. Zhao & Xie (1993)

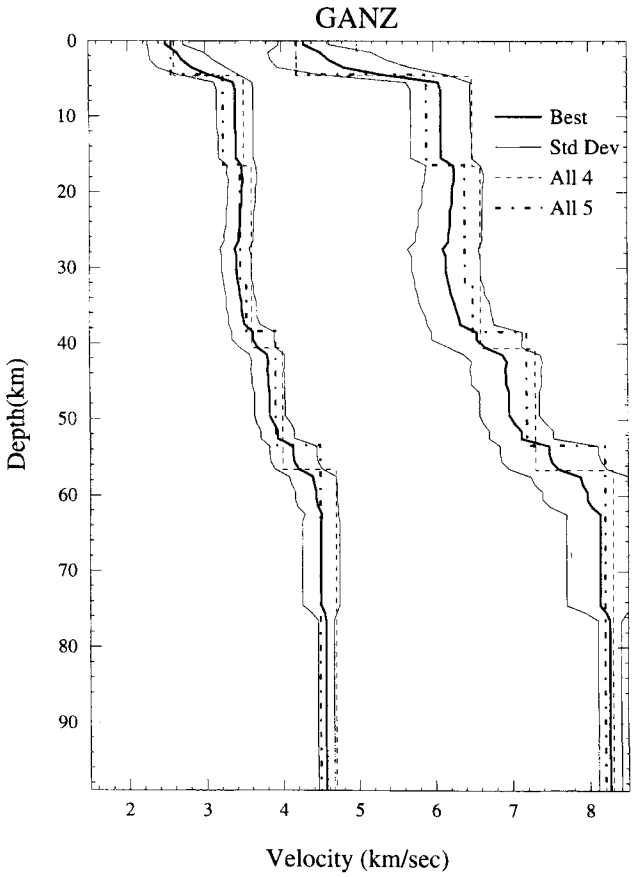

Figure 9. Velocity models obtained for station GANZ.

determined a P_n velocity of 7.8–7.9 km s^{-1}, but provided no information about crustal thickness. We have 12 signals at azimuths of 45°–164° and one at 293°. Five of these waveforms are somewhat noisy.

Beneath ERDO, our principal results are that the crustal thickness is about 70 km, and that the velocity increases with depth; we find no evidence for a low-velocity zone beneath the uppermost crust (Fig. 8). The shear velocity in the uppermost 4 km is quite low, about 2.5–2.6 km s^{-1}, and this overlies a roughly homogeneous layer with a shear velocity of 3.5 km s^{-1} and a thickness of about 30 km. Between 40 and 70 km depth there are two distinct layers, but no sign of a low-velocity zone. The Moho boundary is sharp, as the shear velocity changes from 3.9 to 4.4 km s^{-1} within a few kilometres. Generally, the uncertainty for the mantle shear velocity is small, about $\pm$0.2 km s^{-1}.

Station GANZ

Little is known about the crustal structure beneath station GANZ, which is situated at the edge of the underthrusting Indian plate on the eastern side of the Sino–Franco joint study area (e.g. Yuan *et al.* 1986). Zhao & Xie (1993) found the P_n velocity to be about 7.9 km s^{-1} here. In this study, our VFSA inversion for structure did not perform well, as we were able to obtain only eight signals with an azimuthal range of 44°–165°, and seven of these were noisy.

Nevertheless, the resolution for shear velocity is acceptable (Fig. 9). The reason for acceptable resolution from the noisy data set is that the noise is probably of random nature. Zhao & Frohlich (1996) presented a synthetic test on a random noise of very high level ($\pm$40 per cent); the results proved to be acceptable. We determined that the Moho is shallow, less than about 60 km depth. There is no low-velocity layer apparent. The uppermost crustal layer has a thickness of about 4 km and a shear velocity of 2.7 km s^{-1}. The layer beneath is roughly homogeneous, with a shear velocity of about 3.4–3.5 km s^{-1}, and overlies a layer with a velocity of 3.8–3.9 km s^{-1}.

Station LSA

LSA is a permanent station in the Chinese digital seismic network, thus we chose to evaluate data recorded there instead of at the nearby PASSCAL station LHSA. There have been several previous investigations of the crustal structure beneath or near LSA (e.g. Hirn *et al.* 1984; Teng *et al.* 1983; see summary in Zhao & Xie 1993). Teng *et al.* (1983) reported that there is a low-velocity layer at a depth of about 50 km with a thickness of about 10 km and a P velocity of about 5.3 km s^{-1}. They found that the uppermost crustal layer had a thickness of a few kilometres and a P velocity of 4.6–4.7 km s^{-1}; they reported that just above the Moho, the P velocity is high, about 7.3 km s^{-1}. They also found a P_n velocity of 8.0–8.4 km s^{-1}. The crustal thickness is a little more than 70 km, from deep-seismic-sounding data. Zhao & Xie (1993) concluded that the overall crustal thickness in the Lhasa block is about 70–80 km. For the present study we collected waveforms from 15 earthquakes surrounding LSA (Fig. 10, Table 5) to investigate the receiver structure beneath LSA (Fig. 11).

The principal result of the present study is that the overall crustal thickness is about 70–80 km. In contrast to the suggestion of Teng *et al.* (1983), we find no evidence for a low-velocity layer at about 50 km depth. The uppermost crustal layer has a thickness of about 4 km, overlying a rather homogeneous layer of about 50 km thickness with a shear velocity of 3.3–3.5 km s^{-1}. At greater depths the velocity increases approximately linearly. While the precise thickness of the crust is not well resolved, it is constrained to be in the range of 70–80 km. Generally, the shear velocity is well determined, whereas the P velocity is less so. Overall, the velocity beneath LSA is very slow.

Generally, the fit between observations and synthetics at

Table 5. Events used for the LSA station.

ID	Date mmddyy	Time hhmm	Location (°N, °E)	Depth (km)	Mag (M_b)	Δ (°)	B Az (°)
042	021192	1025	-9.457 124.671	29	5.7	50.6	135
048	021792	0001	79.171 124.540	10	6.0	51.6	8
062	030292	1229	52.884 159.997	44	6.5	54.4	44
073	031392	1718	39.706 39.570	28	6.2	43.1	298
151	053092	1242	30.695 141.620	26	5.9	43.3	76
154	060292	2105	-16.199 92.810	10	5.7	45.7	178
158	060692	2140	1.068 123.971	25	5.8	42.3	126
200	071892	1356	39.466 143.026	21	5.7	43.3	63
253	090992	1308	76.205 7.241	24	5.7	60.0	344
342	120792	0211	43.912 147.145	51	5.9	46.2	56
439	020893	0424	-4.861 101.956	34	5.7	35.9	161
460	030193	0139	-3.729 138.493	117	6.0	56.2	118
472	031393	1712	19.672 38.848	10	5.7	48.2	271
615	080393	1243	28.628 34.644	10	6.0	48.9	283
620	080893	0834	12.964 144.776	60	7.2	52.2	97

Figure 10. Location map of earthquakes (stars) evaluated at station LSA (triangle) in this study.

LSA is very good (Fig. 12), especially for the models determined from individual waveforms. In particular, for nine of the 15 waveforms the difference between observations and synthetics was less than 0.3, and none had a difference of 0.6 or greater. The earthquake with a backazimuth of 344° (Fig. 15) was anomalous, as the fit for the individual model was excellent, but poor for the 'All' model. For this event, while the overall crustal thickness as determined for four- and five-layer models was 66 km, the thickness as determined for all 15 waveforms simultaneously was about 80 km.

Station MAQI

Station MAQI is situated in eastern Tibet where there have been no previous investigations of crustal structure. We collected waveforms of acceptable quality from 11 earthquakes for analysis with the VFSA algorithm.

Beneath MAQI our principal results are that there is a low-velocity zone beneath about 10–20 km depth, and that the total crustal thickness is about 65–75 km (Fig. 13). In the uppermost crust there is a layer about 2 km thick with a shear velocity of about 2.4 km s^{-1}. Beneath this layer, there is a higher-velocity layer with shear velocity greater than 3.7 km s^{-1} and a thickness of about 10 km. Then, at about 25 km depth, the shear velocity reaches a local minimum of about 3.4 km s^{-1}. The low-velocity region extends to about 50 km depth, then beneath this the shear velocity increases roughly linearly down to the Moho. The depth of the Moho is not well resolved, but is in the range of 65–75 km. The resolution for P velocity is poorer than that for shear velocity. The mantle shear velocity is 4.4–4.6 km s^{-1}.

Station SANG

Station SANG is situated close to station LSA within the Sino–Franco study area (e.g. Yuan *et al.* 1986). Previous investigations indicate that the crustal structure is roughly the same as beneath LSA (e.g. Zhao & Xie 1993). We have collected 12 records covering the azimuths between 45° and 161° and one record at 297°; however, seven of these records are somewhat noisy.

Our principal results are that the crustal thickness is 65–75 km, and that there is no evidence for a low-velocity zone (Fig. 14). Generally, the crustal velocities beneath SANG are slow; for the upper 40 km the velocity is about 3.2 ± 0.3 km s^{-1}. Beneath this depth the velocity increases roughly linearly. The Moho is in the depth range 65–75 km. We find that the mantle shear velocity beneath station SANG is slightly higher than that of LSA, and is 4.5–4.7 km s^{-1}. The resolution of the crustal P velocity is relatively poor.

Station TUNL

Station TUNL lies in the southern part of the Qaidam Basin, where previous investigations have found the crustal thickness to be between 50 and 70 km. Zhao & Xie (1993) suggested a 65–70 km thickness, but with a very large uncertainty. Zhu *et al.* (1993) investigated the velocity structure beneath TUNL

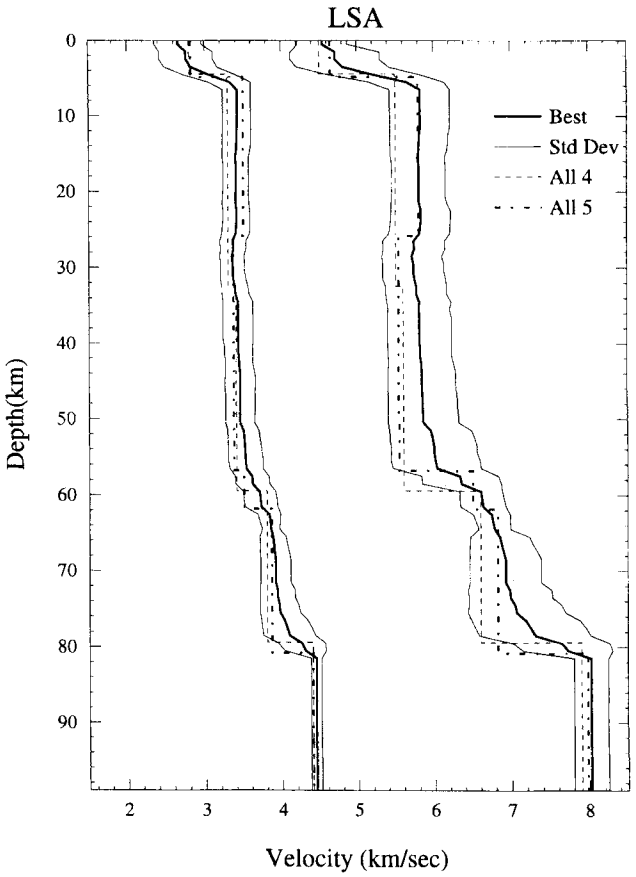

Figure 11. Velocity models obtained for station LSA.

using a receiver-function technique (Owens *et al.* 1984), stacking receiver functions determined from waveforms at backazimuths of about 50° and 130° and distances of about 70°. However, there is a possible problem with stacking *P* waveforms at this distance (Zhao & Frohlich 1996) because of contamination by *PcP* arrivals (the *PcP* ray parameter is 0.038 s km^{-1}, whereas for *P* it is 0.054 s km^{-1}). Zhu *et al.* (1993) obtained a crust with a thickness of about 70 km and a distinct low-velocity zone, with shear velocities of 3.8 km s^{-1} at depths of 17–30 km and 3.5 km s^{-1} at depths of 30–50 km.

Our VFSA analysis of 15 waveforms, two of which are noisy, from azimuths of 8°–292° confirmed the presence of a low-velocity zone and also obtained a crustal thickness of about 70 km (Fig. 15), but the details of the structure we determined are somewhat different from that of Zhu *et al.* (1993). We determined that the uppermost crust beneath TUNL has a low shear velocity of 2.5 km s^{-1} and a thickness of about 1 km, overlying a layer about 10 km thick with a velocity of 3.6–3.7 km s^{-1}. The low-velocity region has a shear velocity of 3.4–3.5 km s^{-1} extending down to about 35 km; below this depth the velocity increases approximately linearly. The Moho is quite sharp, and the mantle shear velocity is 4.4–4.6 km s^{-1}. Thus, the main differences between our 'Best' results (Fig. 15) and those of Zhu *et al.* (1993) are that we find a slower and thinner high-velocity lid overlying the low-velocity region, and we obtain a somewhat thinner low-velocity region. However, the Zhu *et al.* (1993) velocities generally lie within the uncertainty ranges of our analysis.

Station USHU

Station USHU is situated in eastern Tibet, where little is known about the crustal structure. We collected 14 waveforms from events with backazimuths of 7°–264°; five of these waveforms are somewhat noisy.

Our principal results are that the crustal thickness is about 70–80 km, and there is no distinct low-velocity zone within the crust (Fig. 16). The uppermost crust has a low-velocity top about 3 km thick overlying a zone where the velocities are roughly constant down to a depth of 50 km. In this region the shear velocity is 3.5–3.6 $\pm$ 0.2 km s^{-1}, and then, at greater depths, the velocity increases.

Station WNDO

Station WNDO is situated in central Tibet. Zhu *et al.* (1993) studied the receiver structure here, and reported two different models—one for events to the northeast and one for events to the southeast. In their northeast model the Moho is at 68 km depth, and there is a transition zone above it. Velocities within the upper 60 km are quite homogeneous and about 3.4–3.5 km s^{-1}, except that there is a high-velocity lid at depths of 2–15 km with a shear velocity of 3.7–3.8 km s^{-1}. In their southeast model the crustal thickness is 67 km, and there is no high-velocity lid in the uppermost crust. For the present study we collected waveforms for 13 earthquakes with backazimuths from 46°–294°; all of the records were of good quality.

Our principal result is that the crustal thickness beneath WNDO is about 65 km (Fig. 17). The uppermost crustal layer is about 1 km thick, and this overlies a zone about 50 km thick where the shear velocity is about 3.5–3.6 $\pm$ 0.1 km s^{-1}. Generally our results are in agreement with the models of Zhu *et al.* (1993); we also find a transition zone a few kilometres thick situated just above the Moho and a high-velocity lid similar to that in their northeast model from waveforms at backazimuths of 57° and 64°.

Station XIGA

Station XIGA was situated on the Yarlu–Zangbo suture zone until February of 1992, when it stopped operating due to vandalism (Zhu *et al.* 1993). Zhu *et al.* (1993) inverted stacked receiver functions for events in the northeast direction and obtained an overall crustal thickness of 80 km. They found a strong reflector at 20 km depth where the shear velocity increased from 3.5 to 4.0 km s^{-1}; below 30 km the velocity decreased, reaching 3.2 km s^{-1} at about 50 km, and then it increased again at greater depths. Just south of XIGA the Sino–Franco deep-seismic-sounding study determined a crustal thickness of 70–77 km and a P_n velocity of 8.1–8.2 km s^{-1} (see Zhao & Xie 1993 for a summary). Due to a mispick of an unclear P_n arrival, 8.7 km s^{-1} was suggested and consequently anisotropy. Zhao & Xie (1993) suggested a velocity of 7.9 km s^{-1} beneath the station site.

At XIGA we collected only eight events, and all but two of them are noisy. Our principal results at XIGA are that the crustal thickness is about 70–75 km, and that there may be a peculiarly deep low-velocity region at about 40–55 km depth (Fig. 18). The uppermost crust has a low-velocity top about 3 km thick, overlying a 40 km thick region that is roughly homogeneous with a shear velocity of 3.4–3.6 $\pm$ 0.2 km s^{-1}. We did find a reflector at about 20 km depth, but the shear-

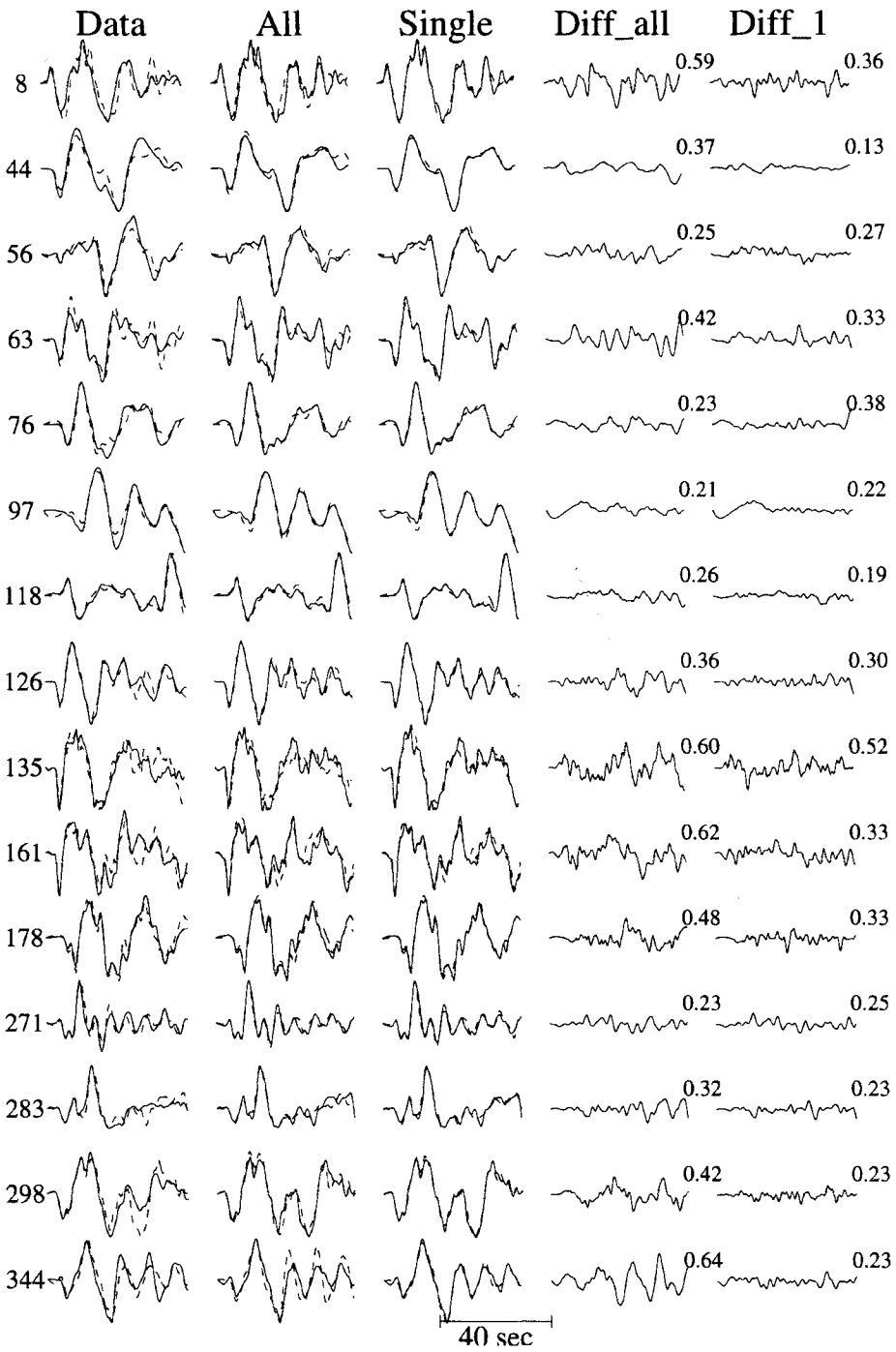

Figure 12. Waveform comparisons for data and synthetics at station LSA. The format is the same as in Fig. 6.

velocity increase there was just 3 per cent, as compared with the more than 10 per cent increase reported by Zhu *et al.* (1993). The low-velocity (3.0–3.2 km s^{-1}) layer at depths of about 50 km was particularly strong for events in the northeast and east, in good agreement with Zhu *et al.* (1993). However, individual models determined from waveforms occurring in other directions do not exhibit this layer.

DISCUSSION AND CONCLUSIONS

This study demonstrates that the VFSA inversion combined with Zhao & Frohlich's (1996) SORVEC provides an effective and efficient scheme for determining crustal structure from teleseismic body-wave waveforms. As the VFSA algorithm only considers a limited number of models (50000 in this study) for each run, one may not find the absolute, global optimum solution; however, it is almost guaranteed that one will obtain a solution close to the optimum. Because the algorithm concentrates more of the search effort in the region of near-optimum solutions, in practice VFSA often determines a better solution than does a classical grid-search approach, since the grid-search approach has to limit the search space. This is especially true when the inversion problem is highly

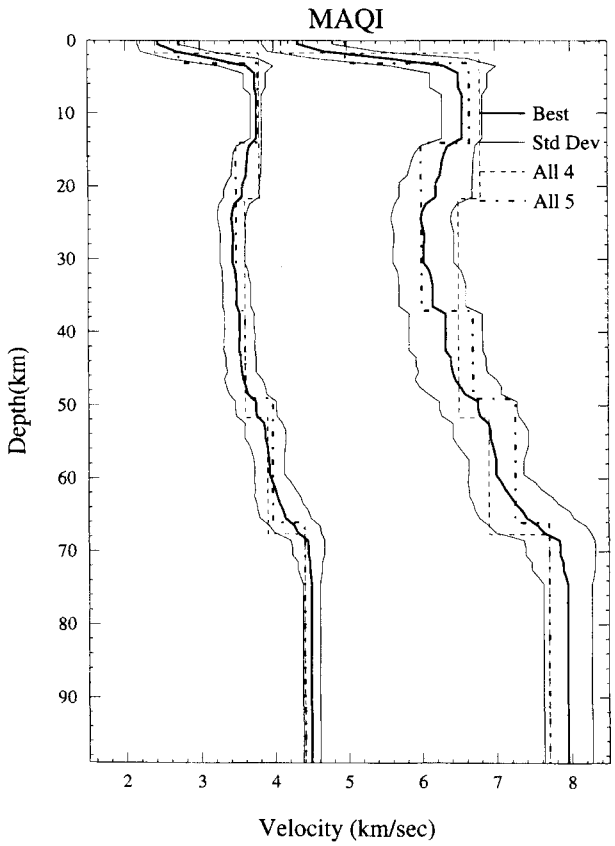

Figure 13. Velocity models obtained for station MAQI.

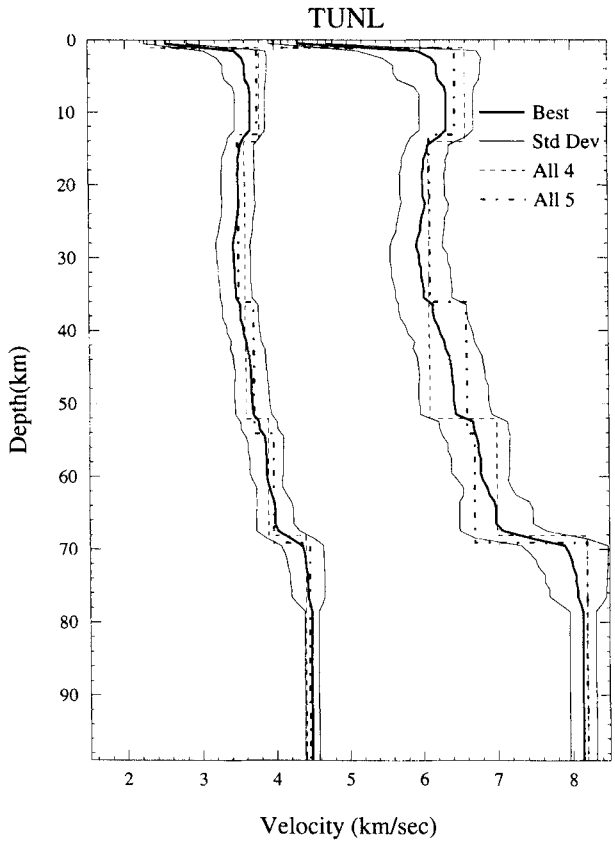

Figure 15. Velocity models obtained for station TUNL.

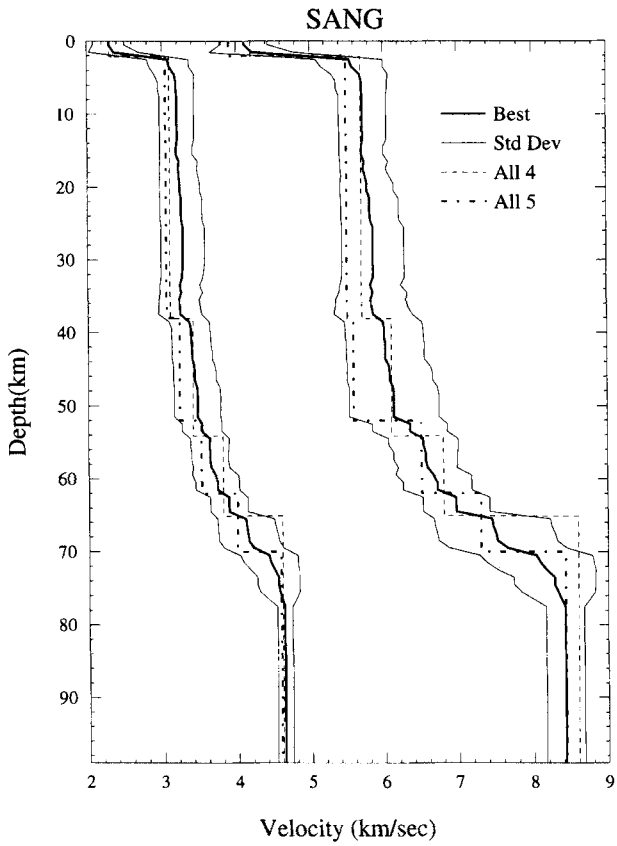

Figure 14. Velocity models obtained for station SANG.

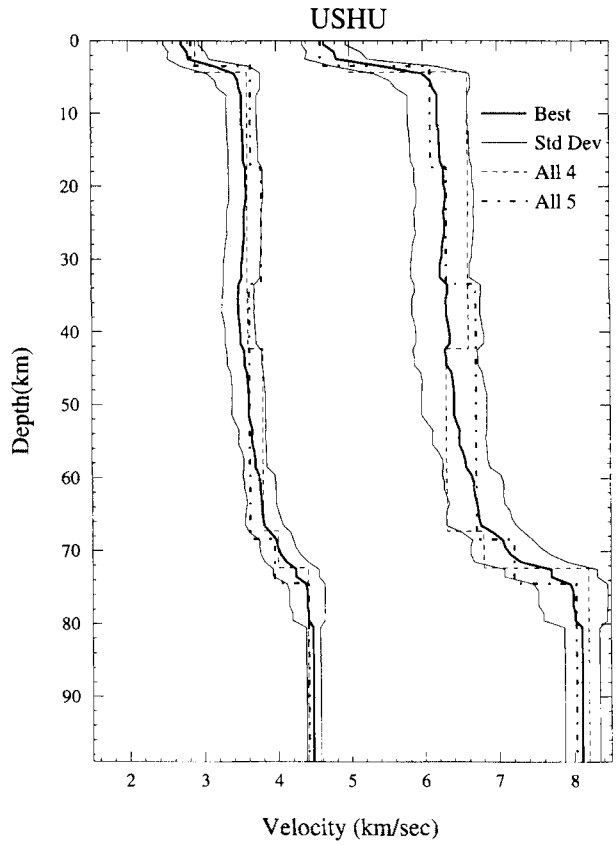

Figure 16. Velocity models obtained for station USHU.

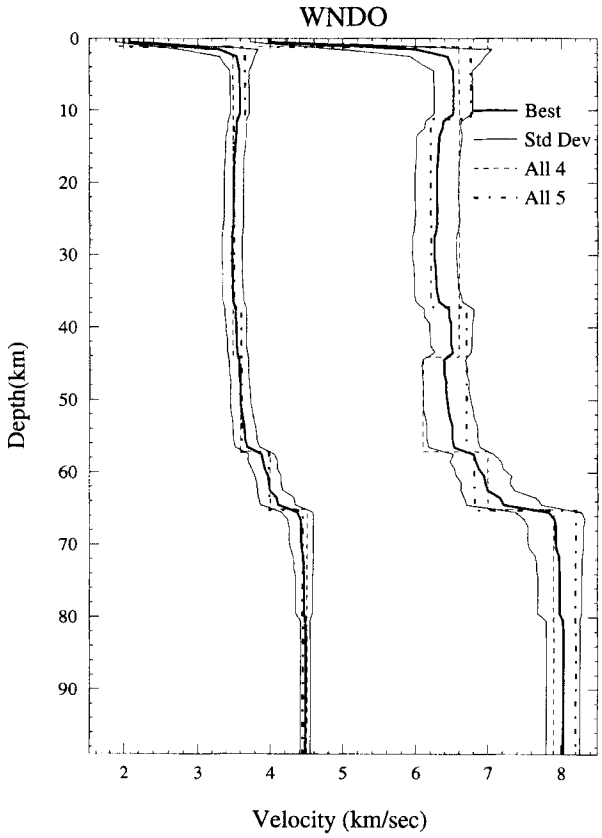

Figure 17. Velocity models obtained for station WNDO.

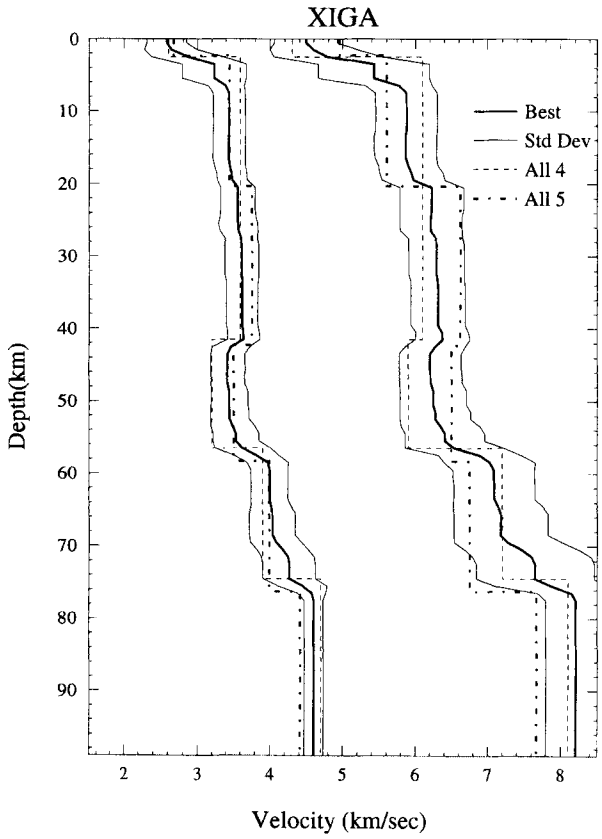

Figure 18. Velocity models obtained for station XIGA.

non-linear, such as with the inversion for layered crustal models, as in this study.

Although the recording duration for the TIBET-PASSCAL stations was 1 yr and some of the stations did not perform well, we were able to obtain very clear results concerning the crustal structure within Tibet (Figs 5, 7–9, 11 and 13–18). It is clear that there is a low-velocity zone in part of Tibet, as suggested by Chun & McEvilly (1986) and Min & Wu (1987). If we separate different crustal regimes by delineating shear velocities from average models of <3.52 ('low-velocity' zone), 3.52–4.0 (lid and middle crust), 4.0–4.3 (crust–mantle transition region) and >4.3 km s^{-1} (Fig. 19), a north–south cross-section demonstrates the nature of crustal variation as we cross Tibet. Overall, the crustal thickness is quite uniform, changing from approximately 68 km to 80 km over a horizontal distance of 700 km. The crust–mantle transition boundary is quite sharp in some regions and more than 10 km thick elsewhere. The bottom of the <3.5 km s^{-1} layer is at 55 km depth in the south, but is about 20 km shallower in the north. The mid-crustal 3.5–4.0 km s^{-1} layer gradually increases in thickness from south to north. Beneath station ERDO, both the upper and middle crusts are thickened, and the Moho boundary swells up. ERDO was at the boundary of north–central Tibet, beneath which the P_n velocity is lower (Zhao & Xie 1993).

From this observation (Fig. 19), it is clear that the geodynamical models that need a weak north Tibet, for example the injection model (Zhao & Morgan 1987), are not supported. Very low velocity in the upper crust agrees with the observation of the absence of long-wavelength topography (Fielding *et al.* 1994). The profile in Fig. 19 also agrees well with the suggestions from the gravity anomaly (Jin, McNutt & Zhu 1994) that the topography of the lithosphere (the crustal thickness or Moho) has a 500 km wavelength.

We speculate that the low-velocity (<3.5 km s^{-1}) layer is a region of higher crustal temperature, where the temperature is produced by frictional heating caused by crustal underthrusting. This would mean that the lower boundary of the low-velocity region (at 55 km depth beneath LSA in the south, and at 36 km beneath TUNL in the north) approximately represents the boundary between the Indian crust and the Eurasian crust. If so, a large part of the upper crust of the Tibetan Plateau is the Indian crust (Fig. 20). Our principal reason for suggesting that the low-velocity region was originally material from the Indian crust is because this zone is thicker in the south beneath LSA and SANG than beneath the northern stations, such as BUDO and TUNL. However, the lower velocity at the south end may also be due partly to its proximity to the zone of collision at the plate boundary, whereas the higher near-surface velocities at the northern end arise because the crust there has had more time to cool. We suggest a geodynamical model for Tibet, as shown in Fig. 20. The Indian plate subducts northwards and the Asian plate subducts southwards (e.g. Zhou *et al.* 1981; Arnaud *et al.* 1992; Willett & Beaumont 1994). An upwelling occurs beneath station ERDO, the convection model as suggested by Houseman, McKenzie & Molnar (1981) and Molnar (1990); see the velocity boundaries depressed in Fig. 19. However, the velocity profile obtained in Fig. 19 does not exclude the possibility of shortening (e.g. Chang *et al.* 1986; Dewey & Bird 1970; Dewey & Burke 1973; England & McKenzie 1982; England & Houseman 1986). The *SKS* splitting observation of McNamara *et al.* (1994) can be understood with east–west

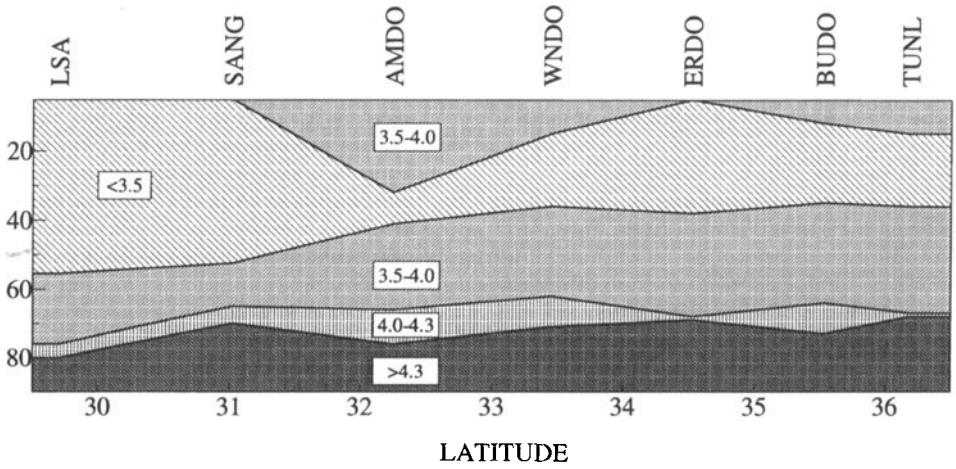

Figure 19. Cross-section summarizing the main features of crustal shear velocity on a south–north transection from LSA to TUNL.

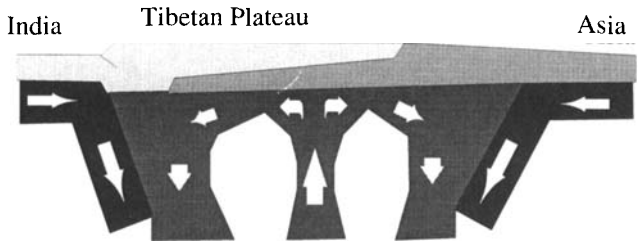

Figure 20. A geodynamical model for Tibet.

movement or strain field; strain heating is also a possibility (Kincaid & Silver 1995).

ACKNOWLEDGMENTS

Partial support for this research was provided by the Air Force Office of Scientific Research under contract F49620-94-0287. All the data used are from the IRIS data center; help from Tim Ahern, Rick Benson, Taoul Titus, and Glynis Wilson is appreciated. This paper is contribution number 1157 of the Institute for Geophysics, the University of Texas at Austin.

REFERENCES

Arnaud, N.O., Vidal, P., Tapponnier, P., Matte, P. & Deng, W.M., 1992. The high K_2O volcanism of northwestern Tibet—geochemistry and tectonic implications, *Earth planet. Sci. Lett.*, **111,** 351–367.

Båth, M., 1974. *Spectral Analysis in Geophysics*, Elsevier Publishing Company, New York.

Chang, C. *et al.* 1986. Preliminary conclusions of the Royal Society and Academia Sinica 1985 geotraverse of Tibet, *Nature*, **323,** 501–507.

Chun, K.-Y. & McEvilly, T.V., 1986. Crustal structure in Tibet: High seismic velocity in the lower crust, *J. geophys. Res.*, **91,** 10 405–10 411.

Dewey, J.F. & Bird, J.N., 1970. Mountain belts and the new global tectonics, *J geophys. Res.*, **75,** 2625–2647.

Dewey, J.F. & Burke, K.C.A., 1973. Tibetan, Variscan, and Precambrian basement reactivation: Products of continental collosion, *J. geol.*, **81,** 683–692.

England, P.C. & Houseman, G.A., 1986. Finite strain calculations of continental deformation, 2. Comparison with the India–Asia collision, *J. geophys. Res.*, **91,** 3664–3676.

England, P.C. & McKenzie, D.P., 1982. A thin viscous sheet model for continental deformation, *Geophys. J. R. astr. Soc.*, **70,** 295–321.

Fielding, E., Isacks, B., Barazangi, M. & Duncan, C., 1994. How flat is Tibet?, *Geology*, **22,** 163–167.

Hirn, A. *et al.* 1984. Crustal structure and variability of the Himalayan border of Tibet, *Nature*, **307,** 23–25.

Houseman, G.A., McKenzie, D.P. & Molnar, P., 1981. Convective instability of a thickened boundary layer and its relevance for the thermal evolution of continental convergent belts, *J. geophys. Res.*, **86,** 6115–6132.

Ingber, L., 1989. Very fast simulated reannealing, *Math. Comput. Model.*, **12,** 967–993.

Jin, Y., McNutt, M.K. & Zhu, Y.-S., 1994. Evidence from gravity and topography data for folding of Tibet, *Nature*, **371,** 669–674.

Kennett, B.L.N. & Engdahl, E.R., 1991. Traveltimes for global earthquake location and phase identification, *Geophys. J. Int.*, **105,** 429–465.

Kincaid, C. & Silver, P., 1995. The orogeny paradox and the role of viscous dissipation, *Science*, submitted.

Kirkpatrick, S., Gelatt, C.D. & Vecchi, M.P., 1983. Optimization by simulated annealing, *Science*, **220,** 671–680.

Langston, C.A., 1979. Structure under Mount Rainier, Washington, inferred from teleseismic body waves, *J. geophys. Res.*, **84,** 4749–4762.

McNamara, D.E., Owens, T.J., Silver, P.G. & Wu, F.T., 1994. Shear wave anisotropy beneath the Tibetan Plateau, *J. geophys. Res.*, **99,** 13 655–13 665.

Metropolis, N., Rosenbluth, A., Rosenbluth, M., Teller, A. & Teller, E., 1953. Equation of state calculations by fast computing machines, *J. Chem. Phys.*, **21,** 1087–1092.

Min, Z. & Wu, F.T., 1987. Nature of the upper crust beneath central Tibet, *Earth planet. Sci. Lett.*, **84,** 204–210.

Molnar, P., 1990. S-wave residuals from earthquakes in the Tibetan region and lateral variations in the upper mantle, *Earth planet. Sci. Lett.*, **101,** 68–77.

Owens, T.J., Zandt, G. & Taylor, S.R., 1984. Seismic evidence for an ancient rift beneath the Cumberland Plateau, Tennessee: A detailed analysis of broadband teleseismic P waveforms, *J. geophys. Res.*, **89,** 7783–7795.

Owens, T.J., Randal, G.E., Wu, F.T. & Zheng, R., 1993. PASSCAL instrument performance during the Tibetan Plateau passive seismic experiment, *Bull seism. Soc. Am.*, **83,** 1959–1970.

Phinney, R.A., 1964. Structure of the Earth's crust from spectral behavior of long-period body waves, *J. geophys. Res.*, **69,** 2997–3017.

Rothman, D.H., 1985. Nonlinear inversion, statistical mechanics, and residual statics estimation, *Geophysics*, **50,** 2784–2796.

Sen, M.K. & Stoffa, P.L., 1991. Nonlinear one-dimensional seismic waveform inversion using simulated annealing, *Geophysics*, **56,** 1624–1638.

Sen, M.K. & Stoffa, P.L., 1995. *Global optimization methods in geophysical inversion.* Elsevier Science Publications, The Netherlands.

Stoffa, P.L. & Sen, M.K., 1991. Nonlinear multiparameter optimization by genetic algorithms: Inversion of plane wave seismograms, *Geophysics*, **56,** 1794–1810.

Tarantola, A., 1987. *Inverse Problem Theory, Methods of Data Fitting and Model Parameter Estimation*, Elsevier Publishing Company, New York.

Teng, J.-W., Sun, K.-Z., Xiong, S.-B., Yin, Z.-X., Yao, H. & Chen, L.-F., 1983. Deep seismic reflection waves and structure of the crust from Dangxung to Yadong on the Xizang Plateau (Tibet), *Phys. Earth planet. Inter.*, **31,** 293–306.

Willett, S.D. & Beaumont, C., 1994. Subduction of Asian lithosphere mantle beneath Tibet inferred from models of continental collision, *Nature*, **369,** 643–645.

Yuan, X., Wang, S., Li, L. & Zhu, J., 1986. A geophysical investigation of deep structure in China, in *Reflection Seismology*, pp. 151–160, eds Barazangi, M. & Brown, L., American Geophysical Union, Washington, DC.

Zhao, L.-S. & Frohlich, C., 1996. Teleseismic body-waveforms and receiver structures beneath seismic stations, *Geophys. J. Int.*, **124,** 525–549.

Zhao, L.-S. & Helmberger, D.V., 1991. Geophysical implications from relocation of Tibetan earthquakes: hot lithosphere, *Geophys. Res. Lett.*, **18,** 2205–2208.

Zhao, L.-S. & Xie, J., 1993. Lateral variations of the compressional velocity structure beneath the Tibetan Plateau from *Pn* travel-time inversion, *Geophys. J. Int.*, **115,** 1070–1084.

Zhao, L.-S., Helmberger, D.V. & Harkrider, D.G., 1991. Shear-velocity structure of the crust and upper mantle beneath the Tibetan Plateau and Southeastern China, *Geophys. J. Int.*, **105,** 713–730.

Zhao, W.-L. & Morgan, J., 1987. Injection of Indian crust into Tibetan lower crust: a two dimensional finite element model study, *Tectonics*, **6,** 489–504.

Zhou, Y.-S., Zhang, Q., Jin, C.W. & Deng, W.M., 1981. The migration and evolution of magmatism and metamorphism in Xizang since the Cretaceous and their relation to the Indian plate motion: A possible model for the uplift of Qinghai-Xizang Plateau, in *Geological and Ecological Studies of Qinhai-Xizang Plateau*, pp. 363–378, Science Press, Beijing.

Zhu, L.P., Zeng, R., Wu, F.T., Owens, T.J. & Randall, G.E., 1993. Preliminary study of crust–upper mantle structure of the Tibetan Plateau by using broadband teleseismic body waveforms, *Acta Seism. Sin.*, **6,** 305–316.